Proof of principle of helium-beam radiography using silicon pixel detectors for energy deposition measurement, identification, and tracking of single ions

Tim Gehrke[a)]
Department of Radiation Oncology, Heidelberg University Hospital, Heidelberg, Germany
Department of Medical Physics in Radiation Oncology, German Cancer Research Center (DKFZ), Heidelberg, Germany
Heidelberg Institute for Radiation Oncology (HIRO), National Center for Radiation Research in Oncology (NCRO), Heidelberg, Germany
Department of Physics and Astronomy, Heidelberg University, Heidelberg, Germany

Raya Gallas*
Department of Medical Physics in Radiation Oncology, German Cancer Research Center (DKFZ), Heidelberg, Germany
Heidelberg Institute for Radiation Oncology (HIRO), National Center for Radiation Research in Oncology (NCRO), Heidelberg, Germany
Department of Physics and Astronomy, Heidelberg University, Heidelberg, Germany

Oliver Jäkel
Department of Radiation Oncology, Heidelberg University Hospital, Heidelberg, Germany
Department of Medical Physics in Radiation Oncology, German Cancer Research Center (DKFZ), Heidelberg, Germany
Heidelberg Institute for Radiation Oncology (HIRO), National Center for Radiation Research in Oncology (NCRO), Heidelberg, Germany
Heidelberg Ion-Beam Therapy Center (HIT), Heidelberg, Germany

Maria Martišíková
Department of Medical Physics in Radiation Oncology, German Cancer Research Center (DKFZ), Heidelberg, Germany
Heidelberg Institute for Radiation Oncology (HIRO), National Center for Radiation Research in Oncology (NCRO), Heidelberg, Germany

(Received 31 May 2017; revised 30 November 2017; accepted for publication 4 December 2017; published 6 January 2018)

Purpose: Hadron therapy has the capability to provide a high dose conformation to tumor regions. However, it requires an accurate target positioning. Thus, the precise monitoring of the patient's anatomical positioning during treatment is desirable. For this purpose, hadron-beam radiography with protons (pRad) and ions (iRad) could be an attractive tool complementing the conventional imaging technologies. On the pathway to an envisaged clinical application, several challenges have to be addressed. Among them are achieving the desired spatial resolution in the presence of multiple Coulomb scattering (MCS), performing radiographs with a sufficient thickness resolution at clinically applicable dose levels, and the search for combinations of particularly suitable hadrons and detectors. These topics are investigated in this work for a detection system based on silicon pixel detectors.

Methods: A method of iRad based on energy deposition measurements in thin layers is introduced. It exploits a detection system consisting of three parallel silicon pixel detectors, which also enables particle tracking and identification. Helium ions, which exhibit less pronounced MCS than protons, were chosen as imaging radiation. A PMMA phantom with a mean water-equivalent thickness (WET) of 192 mm, containing maximal WET-variations of ± 6 mm, was imaged with a 173 MeV/u helium ion beam at the Heidelberg Ion-Beam Therapy Center. WET-differences in form of 2.3 mm $\times$ 2.3 mm steps were aimed to be visualized and resolved in images of the energy deposition measured behind the phantom. The detection system was placed downstream of the imaged object in order to detect single ions leaving it. The combination of the measured information on energy deposition, ion type, and the track behind the phantom was used for the image formation, employing a self-developed data-processing procedure.

Results: It was shown that helium-beam radiography is feasible with the reported detection system. The introduced data preprocessing purified the detector signal from detector artifacts and improved the image quality. Additionally, the rejection of hydrogen ions originating from nuclear interactions was shown to increase the contrast-to-noise ratio (CNR) by at least a factor of 2.5. This enabled the resolution of relative thickness differences of 1.2% at a dose level typical for diagnostic x-ray images. The spatial resolution was improved by taking into account the direction of single helium ions leaving the phantom. A spatial resolution ($MTF_{10\%}$) of at least 1.15p mm^{-1} for the presented experimental set-up was achieved.

Conclusion: A successful feasibility study of helium-beam radiography with the introduced detection system was conducted. The methodology of iRad was based on energy deposition measurements

in thin silicon layers. The tracking of single ions and the method of the ion identification was shown to be important for helium-beam radiography in terms of spatial resolution and CNR. © *2017 American Association of Physicists in Medicine* [https://doi.org/10.1002/mp.12723]

Key words: helium-beam radiography, ion imaging, silicon pixel detectors, secondary particles, particle therapy

1. INTRODUCTION

Hadron[†] therapy can improve cancer treatments due to the high dose conformation to the tumor.[1,2] However, this dose conformation, which intrinsically implies high gradients of the dose profile, also represents a major challenge. A precise planning and alignment of the radiation field with respect to the target is important during the treatment. It requires an accurate determination of the proton/ion stopping power (SP). Currently the SP, which is typically specified relative to water (RSP), is resolved based on a conversion from x-ray attenuation measured during a planning CT. This conversion gives rise to range uncertainties of 3%–3.4%, averaged over different treatment sites.[3,4]

Therefore, direct measurements of the RSP in 3D, for example, by means of proton CT and ion-beam CT (pCT and iCT) would be ideally suited for absolute range verification purposes.[5–7] Proton and ion-beam radiography (pRad and iRad) are technically easier to implement and they have many features that are of great interest in the field of quality assurance for hadron therapy. In principle, the measurement of the integrated RSP along a projection axis through the patient (WET-map) is achievable. Based on that, a long-term goal of our work is to apply iRad for the *in vivo* range verification by comparing an actually measured WET-map with the WET-map based on a digitally reconstructed radiograph from the planning CT (similar to the concept of a range probe[8]). Furthermore, there are several published works concluding that pRad and iRad can deliver a superior density or thickness resolution in comparison to x-ray radiography at the same dose level.[9–11] This is a decisive feature with regard to an application for *in vivo* monitoring of the patient anatomy. pRad and iRad could also be used for a patient-specific optimization of the relation between the CT Hounsfield units and the stopping power.[12,13]

Many promising prototypes of detection systems for pRad/iRad/pCT/iCT have been developed, which can be divided into *integrating* and *tracking systems* following the nomenclature of Poludniowski et al.[7] In both approaches most of the reported prototypes measure the energy loss or the residual energy/range of several or single particles downstream of the object in order to form an image.

Integrating systems measure the integrated signal of the particles downstream of the object being imaged (pRad:[14,15]; iRad:[16]; pCT:[17]; iCT:[16,18–20]). Most of these works focus on the usage of carbon ions due to the less pronounced MCS, which is especially important for non-tracking systems. The reported applied doses for these systems are rather high, for example, 7 mGy for one radiograph[14] or 8 Gy for one CT.[19]

Tracking systems use the track information of single particles by measuring the entrance and exit position. The first *tracking system* was developed at PSI.[21] With the successor of this system, the first pRad of an animal patient was performed by measuring the entrance and exit position of single protons with scintillating fiber hodoscopes and a scintillator range telescope.[9] The pCT Collaboration (Loma Linda University, University of California Santa Cruz, Northern Illinois University, California State University San Bernadino) used silicon strip detectors in order to measure the entrance/exit position and direction[6,22] for the application in pCT. The additional directional information was used in so-called *most likely path* algorithms[23–26] to improve the spatial resolution. There are several further groups, for example, AQUA, PRIMA, and PRaVDA, working on *tracking systems* with a variety of different detection technologies for pCT[27] and pRad.[28,29]

However, there is still no combination of detection system and hadron that has been shown to be optimal for the clinical application of hadron imaging. Topics of ongoing discussion include the choice of suitable hadrons,[30] which influences the spatial resolution and the applied dose, the reduction of the thickness/material budget of the particle trackers that affect the spatial resolution due to MCS,[31] and the use of different detection systems for the energy/range measurement that influence the density resolution.[32,‡]. Therefore, investigations of different implementations with different detection systems are currently of large interest.[7]

The present work reports a method for helium-beam radiography with a detection system consisting of silicon pixel detectors for tracking, identification, and energy deposition measurement of single ions in thin layers. The pixel technology has several unique features. In contrast to silicon strip or scintillating fiber detectors, which require at least two layers for the measurement of the ion position in two dimensions, pixel detectors can measure the position in a single thin layer. This enables a reduction in the total material budget and consequently a reduction of MCS in the detection system. In this work, the total material budget of one layer is below a WET of 0.8 mm. Furthermore, pixel detectors provide an unambiguous position determination in cases where multiple ions hit the detector in the

[†]In this work, the term hadron refers in particular to protons and heavier ions.

[‡]Although Plautz et al.[31] report on a detection system mainly used for pCT, the findings are also valid for pRad and iRad.

same time window. It distinctly facilitates the track reconstruction.

We exploit the steep gradient of the energy deposition proximal to the Bragg peak, so that small differences in the WET of the object can still lead to detectable signal differences at low applied doses. As the region of the steep gradient in the proximal part of the Bragg curve has to be situated within the thin detection layer, the high-density resolution is limited to a certain range of object thickness in this pilot study.

Helium ions as imaging radiation were chosen because their characteristics are particularly suited for hadron-beam radiography. First of all, they undergo less pronounced MCS within the object being imaged than protons. The angular distribution of helium ions that underwent MCS in a medium can be estimated to be half as broad as for protons with the same range, using the Highland-Lynch-Dahl[33,34] formula. Consequently, the spatial resolution of helium-beam radiography can be expected to be higher than for proton radiography, provided that beams with the same range are used. Secondly, the ratio between the energy loss straggling[35] and the energy loss[36,37] for helium ions is shown to be half as large as for protons. As a consequence, the number of helium ions that contribute to the image can be reduced by a factor of four compared with the number of protons in order to achieve the same density resolution.[10] Since the Bragg curves of protons and helium ions essentially only differ by a constant factor of four,[38] the applied dose is expected to be similar for a helium-beam radiograph and a proton radiograph with identical density resolutions.

A challenge of helium-beam radiography is the nuclear fragmentation process of the primary helium ions that takes place within the object being imaged or inside the detection system. The mixing of the decreased energy deposition of the secondary hydrogen ions with the energy deposition of the helium ions would compromise the density resolution. Therefore, it is important to identify and exclude the secondary fragments prior to the image formation.

2. METHODS

We present a method of iRad with a helium beam as imaging radiation. Besides the measurement of the energy deposition, an identification of different ion types (helium ions and light secondary fragments) leaving the phantom being imaged was performed. It allows for a selection of helium ions during the image formation. The measurement of the direction of the single ions behind the phantom was used to mitigate the image degradation due to MCS. The corresponding radiation detection system consisted of three pixelated detection layers, which were placed behind the imaged phantom and were operated in synchronization.

2.A. Imaged phantom and helium-beam irradiations

The imaged phantom is schematically depicted in Fig. 1. It consisted of a 160 mm thick block of acrylic glass (PMMA),

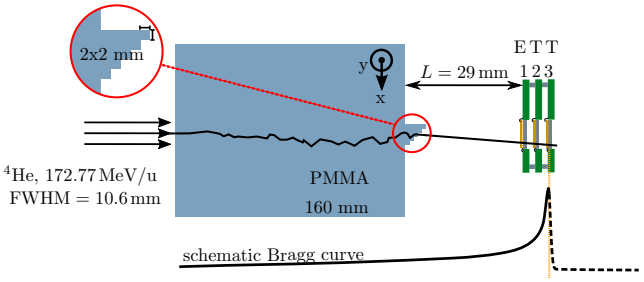

FIG. 1. Schematic view of the experimental set-up. The 2 mm × 2 mm steps behind the 160 mm thick block of PMMA were aimed to be imaged. Depending on the image formation strategy, either the data of detector 1 operated in energy mode (E) or the data of the detectors 1, 2, 3 operated in energy, time, time mode (E T T), respectively, were deployed. [Color figure can be viewed at wileyonlinelibrary.com]

which reflects the head size of a typical patient. Five steps with a step height and width of 2 mm were attached to the beam exit surface. Each of the steps represents a change of 1.2% of the phantom's mean WET. The aim was to image this phantom in a way that the five steps could be resolved at a clinically relevant dose level. The detection system was placed behind the phantom in order to register the ions leaving it. The relatively simple experimental set-up in terms of extent and position of the heterogeneity was chosen in order to provide a proof of principle of performing iRad with the detection system described in Section 2.B.

The reported experiments were performed at the Heidelberg Ion-Beam Therapy Center (HIT).[39] Since 2009 until the end of 2015, approximately 1200 patients have been treated at HIT with protons and 2100 patients with carbon ions.[40] Helium ions and oxygen ions are already available for research purposes. The synchrotron accelerator at HIT enables an active adjustment of the beam energy. Ranges in water from 20 mm to 300 mm are available for protons, helium, and carbon ions.

Helium ions were chosen as imaging radiation due to the expected better spatial resolution in comparison to protons. They were accelerated to a kinetic energy of 172.77 MeV/u, which assured that the vast majority of unfragmented ions could penetrate the complete detection system, positioned downstream of the phantom in the rising part of the Bragg peak. To find a trade-off between a very steep but narrow proximal part of the Bragg peak (high WET-resolution in a small WET-range) and a less steep but broadened Bragg peak (lower WET-resolution in a wider region), a ripple filter was used. The ripple filter contained PMMA-equivalent thickness modulations between 0.3 mm and 3 mm.[41] The irradiation was performed with a single pencil beam with a width of 10.6 mm (FWHM) in air at the isocenter (without the phantom), leading to a sufficiently homogeneous coverage of the detectors' sensitive area of 14 mm × 14 mm. To minimize an overlap of signals from different ions at the detector, the fluence rate was decreased from the lowest therapeutically used fluence rate of approx. $8\times10^4\text{mm}^{-2}\text{s}^{-1}$ to $3.1\times10^2\text{mm}^{-2}\text{s}^{-1}$. The utilized fluence rate was measured by the detection system, averaging over the detector area and over timespans, where both the synchrotron and the detection

system were active (i.e., not during spill pauses or detector dead times).

2.B. Radiation detection system composed of Timepix detectors

The radiation detection system was composed of three synchronized Timepix detectors[§] in parallel alignment and was placed downstream of the phantom being imaged, as shown in Fig. 1.

2.B.1. Timepix detector

The semiconductor pixel detector Timepix was developed within the Medipix2 Collaboration at CERN.[42] It has a sensitive area of 14 mm × 14 mm, which is pixelated into 256 × 256 pixels with a pixel pitch of 55 μm. Each pixel has its own electronic circuit on the application-specific integrated circuit (ASIC) of the detector. In order to reduce the MCS within the detection system to a minimum, a thinned Timepix ASIC of approximately 100 μm was used. A silicon sensor layer with a thickness of 300 μm was attached to the ASIC and a reverse bias voltage of 10 V was applied. The choice of the bias voltage was optimized for energy deposition measurements and is explained elsewhere in detail.[43] For detector operation and data acquisition, the readout interface FitPIX was deployed.[44] It enabled the synchronized operation of the Timepix chips.[45] This means that the time windows of data acquisition (active times) of the three detectors were started and stopped simultaneously. An active time is also called frame, which is followed by a dead time of the detector required for the electronic readout. With three detectors attached to a single FitPIX, a readout rate of approximately 12 frames per second via USB 2.0 could be achieved. The acquisition time of the frames was set to 1 ms. The readout rate, acquisition time, and fluence rate led to a particle detection rate of approximately 4 $mm^{-2}s^{-1}$ or 800 Hz for the whole sensitive area of 196 mm^2. The software Pixet (Version 1.4.2)[46] was used for setting the measurement parameters, controlling the data acquisition, online visualization, and saving of the measurement data.

The detector enables the detection of single particles, in case their energy deposition is high enough to exceed the user-defined threshold. The threshold of the detectors was set to 5 keV by means of a threshold calibration using x-ray emission lines and allowed noise-free measurements. Dependent on the chosen detection mode, each pixel can measure the arrival time (time mode) or the energy deposition (energy mode) of the incident particle radiation.[42] When a pixel is operated in time mode, an external clock with a frequency of 10 MHz continuously increments a digital counter as soon as the preamplifier signal has risen above threshold till the end of the acquisition. The counter value indicates the time of arrival (ToA) with a resolution of 100 ns. Operated in energy mode, the counter is continuously incremented as long as the preamplifier signal is above threshold and indicates the Time over Threshold (ToT) of the respective pixel. As each pixel has its own electronic circuit, the calibration between the ToT and the energy deposition has to be performed separately for all the 65536 pixels. The threshold setting and the pixel-by-pixel calibration was performed by the company Advacam[41] using x-ray radiation of different energies.[47]

When a heavy charged particle impacts onto the detector, the generated signal spreads over several pixels.[48] An ensemble of adjacent pixels, having a nonzero signal at the end of an acquisition time, is called cluster. Excerpts of two typical acquisition frames, one in energy mode and the other one in time mode, are shown in Fig. 2. The term cluster size denotes the number of pixels within a cluster. Other important cluster characteristics for this work are the cluster height and cluster volume. The cluster height specifies the highest pixel value given in ADC counts within a cluster and, measuring in time mode, defines the ToA of the cluster. If operated in energy mode, the cluster volume is the sum of the ToT values within the cluster. The measured cluster volume can be converted into the energy deposition of the incident particle by means of the pixel-wise calibration.

2.B.2. Tracking of single ions

The energy deposition is the basic quantity for the radiography. The time of arrival, when measured by at least two layers, enables the determination of the tracks of single ions. Three parallel Timepix detectors were operated in synchronization. Detector 1 was operated in energy mode and detector 2 & 3 in time mode.

The following *matching algorithm*, implemented in Matlab, was used to combine the information from the three detectors on a single particle basis. Before starting to match the signals by one particle, overlapping clusters on detector 2 & 3 were excluded. Since overlapping clusters are caused by two independent particles, they were identified on the time detectors by their increased standard deviation of the ToA and were rejected. It led to a reduction of approximately 10% of the measured clusters.

In the next step of the *matching algorithm*, the ToA information of clusters measured by detector 2 & 3 was scanned for coincident hits with a coincidence window of 400 ns. Coincidences with either one or two hits on both detectors were considered in the building of tracks. Coincidences with one hit on one detector and two hits on the other detector (5% of all coincidences) due to, for example, nuclear fragmentation processes in detector 2 were excluded. Each track was then extrapolated onto the energy detector plane (det. 1). In case a cluster on the energy detector was found within a distance of 5 pixels (275 μm) to the extrapolated position, it was linked with the track and the corresponding arrival time.

[§]The detectors were purchased from ADVACAM s.r.o., Na Balkane 2075/70, 130 00 Praha 3, Czech Republic, http://www.advacam.com

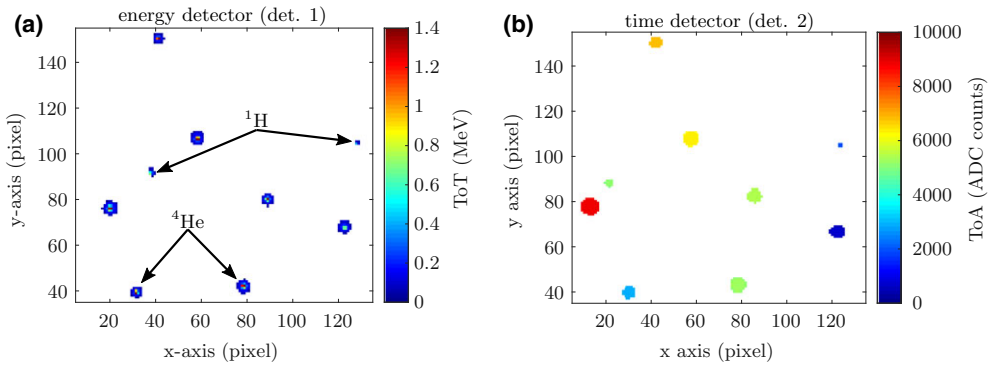

FIG. 2. (a) Excerpt of a typical acquisition frame measured by the energy detector (det. 1). Typical signals, either caused by helium ions or hydrogen ions, are indicated. (b) Excerpt of the corresponding acquisition frame measured by the first time detector (det. 2). [Color figure can be viewed at wileyonlinelibrary.com]

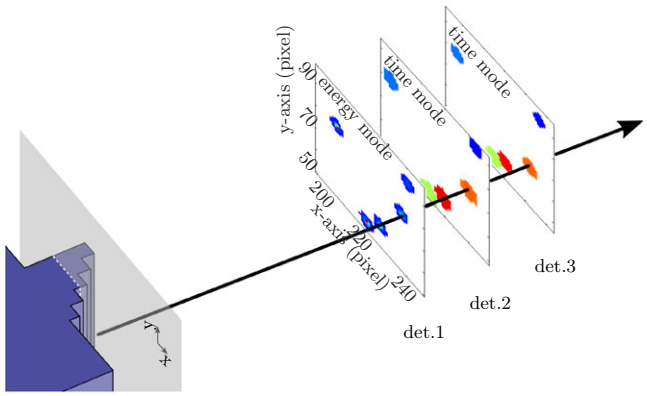

FIG. 3. Schematic illustration of the backprojection algorithm. The last two detectors, operated in time mode, measure the arrival time of the incident ions, indicated as the color of the clusters. Two clusters exhibiting the same arrival time are assigned to one ion. The expected position of this ion on the energy detector is determined by backprojection along the ion track (black line). If a cluster matches the expected position, a backprojection into the *x*-*y*-plane of interest at the rear of the phantom (gray plane) will be performed. [Color figure can be viewed at wileyonlinelibrary.com]

The procedure is illustrated in Fig. 3. The events with linked clusters on all three detectors are referred to as *matched events* in the following.

2.C. Data processing

The measured raw data consist of clusters from the three Timepix detectors. The aim of the developed data-preprocessing and image formation method, described in Section 2.C.1 and 2.C.2. was to exploit the cluster information most effectively in order to create a radiographic image of the PMMA phantom, resolving its 2 mm × 2 mm steps. The data preprocessing consists of four steps (see (1)–(4) below) mainly focused on the filtering of signals with degraded information due to the electronic readout. The subsequent image formation consists of two further steps (see (5)–(6) in Section 2.C.2). After these six processing steps, each pixel of the final radiographic image will represent the mean cluster volume of the clusters measured by detector 1, whose center of mass lies within that pixel.

2.C.1. Data-preprocessing procedure

Desirable signals for the image formation were clusters that were caused by single incident ions traversing all three detector layers resulting in a *matched event*. However, the measured raw data also contained clusters with degraded volume or size information due to overlapping signals from multiple ions, incomplete readout or detector artifacts. These clusters impair the image quality and the aim of the preprocessing procedure was to exclude them prior to the image formation.

Two-dimensional histograms, showing clusters distributed according to their cluster size on one axis and to the cluster volume on the second axis, were found to be useful for identifying the clusters caused by detector artifacts or the clusters with degraded information due to incomplete readout. Figure 4(a) shows the 2D histogram for all clusters measured by the energy detector (det. 1), including contributions of single primary helium ions (I), secondary hydrogen ions from nuclear fragmentations (II) and helium ions that stopped within the energy detector due to the spread of the initial energy and the range straggling (III). Other contributions result from overlapping clusters, caused by two or more ions (IV), from clusters corresponding to ions, whose cluster size and/or volume was degraded due to spatial or temporal clipping at the edges of the sensor or at the beginning/end of the acquisition time, respectively (V, VI, VII). The last cluster type (VIII) is not caused by an incident ion but could be identified as a detector artifact called *overshoot cluster*. They occur after the incidence of an ion with a high energy deposition that leads to pixel signals exceeding approximately 1 MeV and causing overshoot oscillations in the electronics, which can rise above the threshold.[49] Four preprocessing steps were developed in order to purify the raw data sample from the undesired signals related to detector processes (III – VIII).

(1). Overlapping clusters [contribution IV in Fig. 4(a)] measured by detector 1, operated in energy mode, were identified by two or more local maxima within the cluster and were subsequently rejected. The fraction of the rejected overlapping clusters was 10% for the reported measurement.

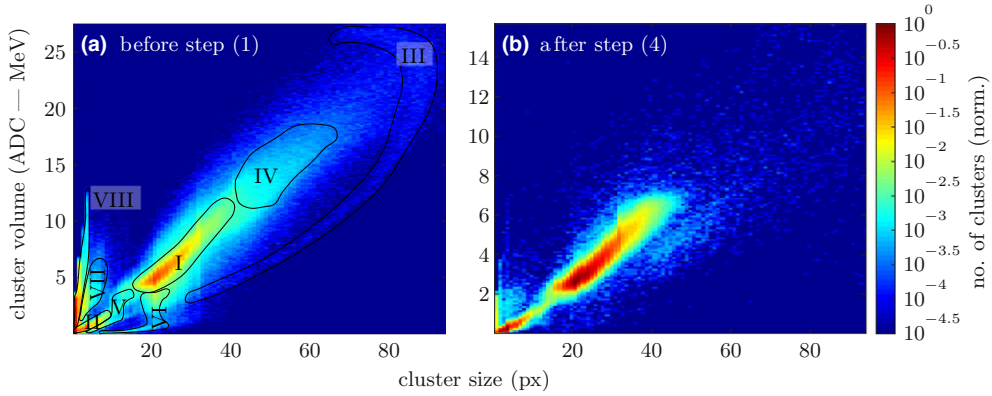

FIG. 4. Distribution of the measured clusters in the parameters cluster size and volume. (a) 2D histogram of all clusters measured by the energy detector. (b) Remaining clusters after the calibration and the removal of clusters with multiple local maxima, of spatially cropped clusters, of temporally cropped clusters, and of so-called overshoot clusters [after step (4)]. [Color figure can be viewed at wileyonlinelibrary.com]

(2). In order to convert the measured ToT into the corresponding energy deposition, the calibration of the signal measured by the energy detector was performed.[47] The calibration also improves the homogeneity of the detector response over the whole pixel matrix.

(3). Spatially cropped clusters (V) at the edges of the sensor on the energy detector were neglected. The vast majority (99%) of the helium ion clusters exhibits a cluster radius below 4 pixels. Hence, rejecting clusters that have their center of mass closer than 4 pixels to the edges is sufficient to exclude spatially cropped clusters from the further analysis.

(4). After step (3), three types of clusters with degraded energy deposition measurements are remaining, which diminish the image quality. There are temporally cropped clusters at the end of a frame (VI), at the beginning of a frame (VII), and the so-called overshoot clusters (VIII). These contributions could be clearly identified and rejected by taking into account the information about their arrival time. The ToA is obtained for each *matched event* (see Section 2.B.2) by detector 2 & 3 in time mode. In order to reject temporally clipped clusters at the end of the acquisition time, *matched events* showing the same uncalibrated cluster height (the highest pixel value in ADC counts within a cluster) on the energy detector and on the time detectors were discarded. The reasoning is that an equality between the highest uncalibrated ToT and the ToA of a *matched event* indicates that the ToT-signal is still above threshold at the end of the frame and not fully read out. Moreover, *matched events* with an arrival time higher than 9950 ADC counts were neglected in order to remove clusters that are possibly clipped due to their arrival before the beginning of the frame. The total fraction of temporally clipped clusters was 13%.
Most of the so called *overshoot clusters* were rejected by applying the matching algorithm. They do not occur in coincidence, since the overshoot oscillation in the preamplifier signal differs for each pixel. The *matching algorithm* also removed clusters of ions already stopping inside the energy detector (III), which therefore do not have an associated track measured in the two time detectors.

The efficiency of the data-preprocessing procedure can be seen in Fig. 4(b), in which the contributions (III)-(VIII) are significantly reduced compared to Fig. 4(a).

2.C.2. Image formation

After filtering of the clusters with degraded information due to the electronic readout, two final steps for the image formation were conducted.

(5). Two main cluster types remained after the completion of the preprocessing and can be distinguished in Figs. 4(b) and 5(a). They are caused by primary helium ions and secondary hydrogen ions, which traversed all three detectors and could be composed to a *matched event*. To select only clusters corresponding to helium ions, clusters with a volume or size below the respective threshold, defined as minimum between the two peaks shown in Fig. 5(b), were rejected since they can be associated with hydrogen ions.
The image quality was found to be further improved by rejecting outliers, that is, clusters with extreme cluster volume and/or size. Outliers were defined as contributions of the 2D histogram, whose frequencies are smaller than a threshold of 2% of the highest frequency. Figure 5(a) indicates this threshold as dashed line and the final selection of clusters as opaque peak.

(6). In order to minimize the blur of the image due to deflections of the helium ions behind the phantom that are caused by MCS within the phantom, the measured directions of the ions behind the phantom were taken into account. A backprojection of the measured

track toward the rear of the phantom into the *x*-*y*-plane was performed, as shown in Fig. 3. Hence, each pixel of the final radiographic image represents the mean cluster volume of the clusters with a back-projected center of mass lying within that pixel. While for the tracking the fine intrinsic pixelation of the detection system was exploited, for the image formation four by four detector pixels were merged to super pixels with a size of 220 μm × 220 μm, which still corresponds to a high granularity in the field of medical radiography.

2.D. Quantitative evaluation of the image quality

2.D.1. Contrast-to-noise ratio

The contrast-to-noise ratio (CNR), as a measure of the thickness resolution, was calculated for images obtained at different stages of the image formation process. The CNR is defined as

$$CNR = \frac{|\langle S_1\rangle - \langle S_2\rangle|}{\sqrt{\sigma_{S_1}^2 + \sigma_{S_2}^2}}, \quad (1)$$

whereas $\langle S\rangle$ and σ_S are the mean and the standard deviation of the pixel values within two homogeneous regions of interest. The CNR was evaluated at the step transitions, where S_1, σ_{S_1} and S_2, σ_{S_2} were determined in four different pairs of ROIs that are left and right of a step transition. For an accurate CNR determination, the transition region itself and the borders of the image were excluded. The mean and the standard uncertainty of the four resulting CNR values were used as the final measure of CNR and statistical uncertainty, respectively.

2.D.2. Spatial resolution

The spatial resolution of the measured images was evaluated by analyzing the step transitions caused by the 2.3 mm × 2.3 mm WET-inhomogeneities of the phantom. To increase the precision of the evaluation, oversampled integrated edge profiles of the step transitions were generated as proposed by Fujita et al.[50] For this, the steps of the phantom were slightly tilted by approximately 1° with respect to the pixel matrix of the detection system. The obtained edge-spread-functions (ESFs) were fitted with a four-parameter error function. Calculating the derivative of the fitted ESF provided the line-spread-function (LSF). The LSF was then transformed into the corresponding modulation transfer function (MTF) by using the following equation $\mathrm{MTF} = |\mathcal{F}\{\mathrm{LSF}\}|/|\mathcal{F}\{\mathrm{LSF}\}|_{v=0}|$, where $\mathcal{F}$ is the discrete Fourier transformation and v the spatial frequency. The spatial frequency (unit: lp mm^{-1}), at which 10 % of MTF(0) is reached, is referred to as $\mathrm{MTF}_{10\%}$.[31,51] The mean $\mathrm{MTF}_{10\%}$ over four independent images was used as the final measure of the spatial resolution in this work.

2.E. Dose calculation

In order to estimate the delivered dose to the PMMA phantom during the acquisition of the helium-beam radiograph, a Monte Carlo (MC) simulation with FLUKA[52,53] was performed. The parameters of the helium ion beam, the geometry of the phantom, and the detection system were implemented in accordance with the measurements. Ion type, energy deposition, and positions in the pixel matrices of the three detection layers were scored for the impinging ions on an event-by-event basis. This approach enabled the simulation of the *matching algorithm* (see Section 2.B.2) and thus the fraction of *matched events* that were assigned to helium ions (*matched helium events*). The number of simulated primaries that entered the phantom within the lateral dimensions of the detector was then scaled so that the number of *matched helium events* was equal for measurement and simulation. A ratio of 45% between the number of *matched helium events* and the number of incoming primaries was observed. The related particle losses are mainly given by nuclear fragmentations in the phantom and by the small geometrical acceptance of the detector used in this work. The scoring of the dose was performed within a region of the PMMA phantom centered at the beam axis. It had the same lateral dimensions as the obtained radiographic image and included the whole length of the phantom (14 mm × 14 mm × 170 mm). It should be

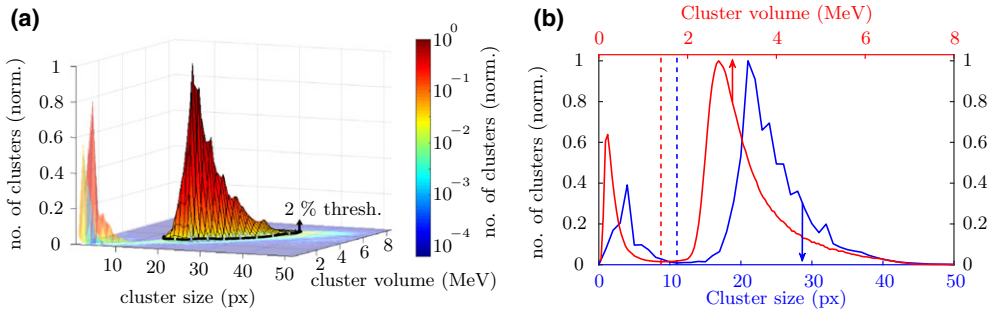

FIG. 5. (a) 2D histogram of clusters on the energy detector after the rejection of clusters with incomplete readout and artifact clusters [after step (4)]. The central peak (opaque colors) indicates helium ions, the smaller peak (transparent color) secondary ions. The color scale and the third dimension is a logarithmic and a linear scale, respectively. (b) Projection of the 2D histogram from panel (a) onto the cluster size axis (lower, blue x-axis) and the cluster volume axis (upper, red x-axis). The dashed vertical lines indicate the minimum between the contribution of the secondary ions and the helium ions, which were used as boundaries between helium and secondary ions. [Color figure can be viewed at wileyonlinelibrary.com]

noted that the dose calculation represents an optimally achievable dose, assuming that the ion beam delivery is interrupted during the dead times of the detection system (see Section 4). The experimentally observed losses in the detector efficiency of about 23% due to effects of the electronic readout (temporally cropped and overlapping signals) would further add to the dose.

To set the required dose for the helium-beam radiograph in relation to currently clinically applied doses, the mean dose within the used PMMA phantom for a typical diagnostic x-ray radiograph was used for a comparison. It was determined as follows. The reference dose area product (DAP) of a diagnostic lateral x-ray projection of an adult skull is 50 μGy m^2.[54] From this DAP, the entrance dose D_E was calculated to be 1440 μGy using the following equation [51, page 379 ff.]

$$D_E = B\frac{(\mu_{en}/\rho)_{PMMA}}{(\mu_{en}/\rho)_{Air}}\frac{DAP}{A}, \quad (2)$$

where A is the irradiated area of the phantom, B is the backscatter factor of 1.38 according to the study of Benmakhlouf et al.,[55] $(\mu_{en}/\rho)_{PMMA}$ and $(\mu_{en}/\rho)_{Air}$ are the mass energy-absorption coefficients for PMMA and air for photons with an energy of 30 keV, respectively.[56,¶] The dose profile of the x-ray field along the depth of the PMMA phantom was obtained by performing a MC simulation with FLUKA. Transport and production thresholds for electrons and photons were set to 1 keV and the dose profile along the depth of the phantom was scored in a 14 mm × 14 mm × 170 mm region centered at the beam axis.

3. RESULTS

Six radiographs of the PMMA step phantom obtained at six different stages of the data processing (Sections 2.C.1, 2.C.2) are depicted in Fig. 6.

Figure 6(a) shows the image, constituted of all the measured raw data before step (1). One vertical stripe with a high mean cluster volume on the left side of the image and a decrease toward higher x-values is visible. This decrease in the mean cluster volume from left to right reflects the expected gradient due to the decreasing PMMA thickness of the imaged object. The unexpected increased cluster volume between y = 20 px and y = 50 px is caused by an increased density of overlapping clusters, which in turn is caused by the nonuniform distribution of the fluence rate of the pencil beam. Furthermore, the WET resolution and the spatial resolution are obviously not sufficient in order to resolve the five steps of 2 mm × 2 mm.

Figure 6(b) shows the radiography, after performing processing step (1) to (4). The increased thickness of the vertical stripes in the middle of the image was reduced by the rejection of overlapping clusters in step (1). After the calibration of the measured cluster volume, performed in step (2), the mean energy deposition is given in units of MeV. The empty pixels at the edges of the sensitive area are caused by the removal of spatially cropped clusters in step (3). In step (4), overshoot clusters and temporally cropped clusters were rejected. Therefore, this image consists only of clusters measured by the energy detector, which can be assigned to *matched events* of primary helium ions or secondary ions. Although the rejection of detector artifacts and clusters with incomplete readout could improve the image, the quality in terms of contrast, noise, and spatial resolution is not sufficient in order to recognize the five PMMA steps of the phantom.

Figure 6(c) depicts the radiography with clusters only originating from helium ions [after processing step (5)]. A comparison with Fig. 6(b) shows that the noise of the image is remarkably reduced by the rejection of clusters caused by secondary hydrogen ions, which gave rise to strong fluctuations in the pixels' mean cluster volume beforehand. However, the spatial resolution is still not sufficient to resolve the 2 mm wide steps of the images object.

Figure 6(d) shows the radiography after the consideration of the measured directional information [processing step (6)] but without excluding the hydrogen ions [without processing step (5)]. With the consideration of the directional information we were able to mitigate the image blurring caused by the angle of the ions with respect to the beam axis behind the phantom. The spatial resolution is distinctly improved as the 2 mm wide PMMA steps in Fig. 6(d) are distinguishable now. The noise of the image is higher than in the image of Fig. 6(c) due to the signal of hydrogen ions, which was already identified as important source of noise.

Figure 6(e) shows the radiography after both the exclusion of the secondary ions [processing step (5)] and the consideration of the measured directional information of the single helium ions [processing step (6)]. The reduced noise of Fig. 6(c) is combined with the improved spatial resolution of Fig. 6(d).

In the previous images (a)–(e), the whole dataset of the measurement was used in order show how the data-preprocessing and the image formation strategies could improve the images at a fixed dose level irrespectively of its magnitude. The calculation of the dose based on MC simulations as described in Section 2.E yields a mean dose of 2.2 mGy within the irradiated volume. This applied dose is too high for a possible clinical application, since the mean dose for a typical diagnostic head x-ray projection was calculated to be 350 μGy in the investigated phantom (see Section 2.E). Figure 6 (f) shows the obtained helium-beam radiograph after the reduction of the dose to 350 μGy by adjusting the number of *matched helium events* from 4.8 × 10^5 to 7.8 × 10^4 in the postprocessing. The five PMMA steps within the image can still be recognized. It shows that a thickness resolution of 1.2% (i.e., 2 mm steps at a maximal overall thickness of 170 mm) over a WET range of approximately 10 mm × $WEPL_{PMMA}$≈11.7 mm can be achieved at a dose level of diagnostic x-ray images. Note that these findings are

¶D_E was calculated for the following parameters. Tube voltage: 70 kVp, mean photon energy: 30 keV , source-to-phantom distance: 705 mm, opening angle: 7° for a quadratic aperture.

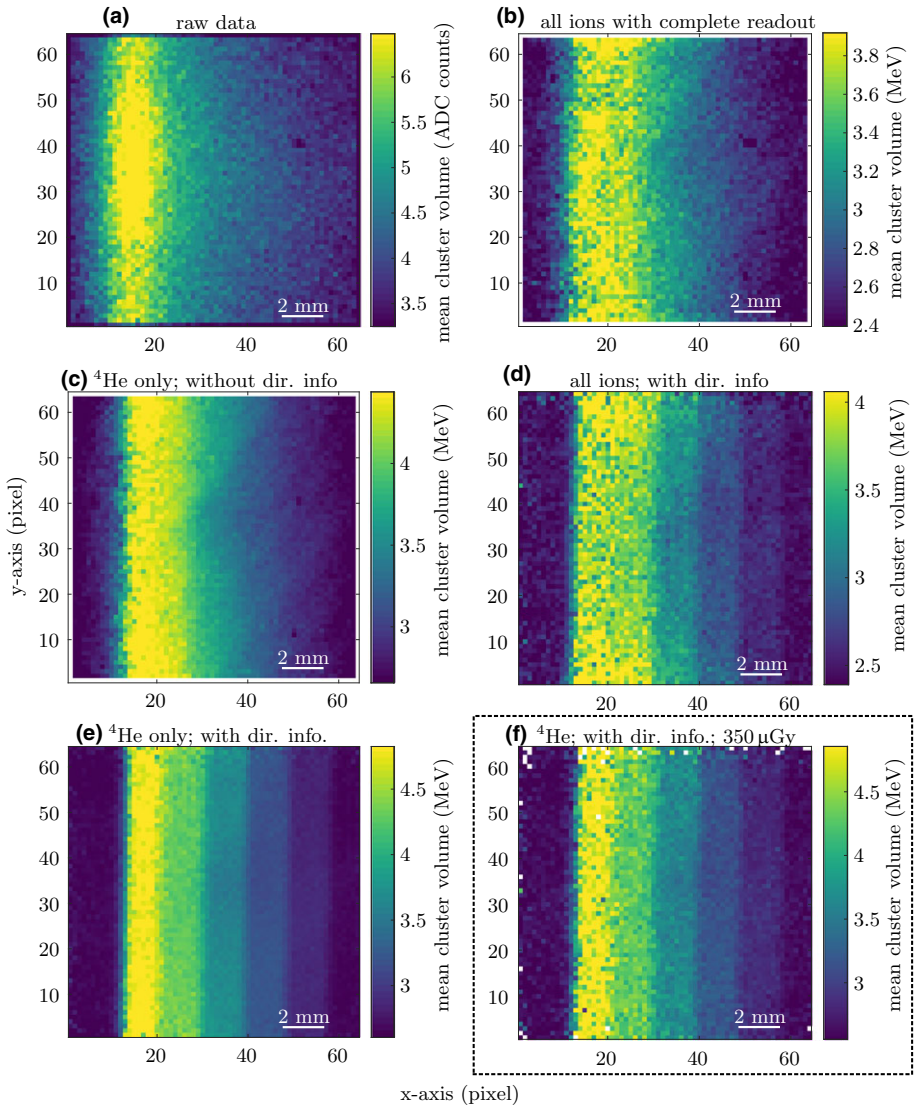

FIG. 6. Measured radiographs showing the PMMA step phantom with a pixel size of 220 µm × 220 µm. They were generated (a) with the raw data of the measurement [before processing step (1)], (b) with all ions [after step (4)], (c) with helium ions only [after step (5)], (d) with all ions after the backprojection [after step (6) w/o performing step (5)], (e) with helium ions after the backprojection [after step (6)] and (f) with a reduced dataset corresponding to a mean dose of 350 µGy. [Color figure can be viewed at wileyonlinelibrary.com]

based on measurements with a mostly homogeneous phantom. Figure 7 depicts a comparison of the radiographs from Fig. 6(c)–6(f) in terms of averaged line-profiles through the images along the *x*-axis. It shows the reduction in the noise due to the selection of clusters caused by helium ions only [processing step (5)]. This is also recognizable by comparing the CNR values of the images with and without the exclusion of the secondary ions (both with consideration of directional information), which are specified in Table I. The CNR of the image with helium ion selection is at least 2.5 times higher than for the image without selection. The CNR values of the image performed at a dose level of 350 µGy are especially high at the three step edges in the middle of the image (CNR > 3.5) and at all step edges above 1.7. For the image obtained without consideration of the directional information, the CNR was not determined due to the absence of homogeneous ROIs. By comparing the sharpness of the edge transitions in Fig. 7, one can see that the spatial resolution of the image with the consideration of the directional information is improved compared to the image obtained without tracking. The $MTF_{10\%}$ as a measure of the spatial resolution is given in Table I and shows a minimal value of 1.15 lp mm^{-1} for the images of this particular phantom with ion tracking. The spatial resolution of the images without tracking cannot be quantified as the five-step transitions are not visible in the image. This is because the ESF is so wide that the step transitions fuse, which prevents its determination.

4. DISCUSSION AND OUTLOOK

The present work demonstrates a proof of principle of helium-beam radiography based on the measurement of energy deposition in thin layers, tracking, and ion

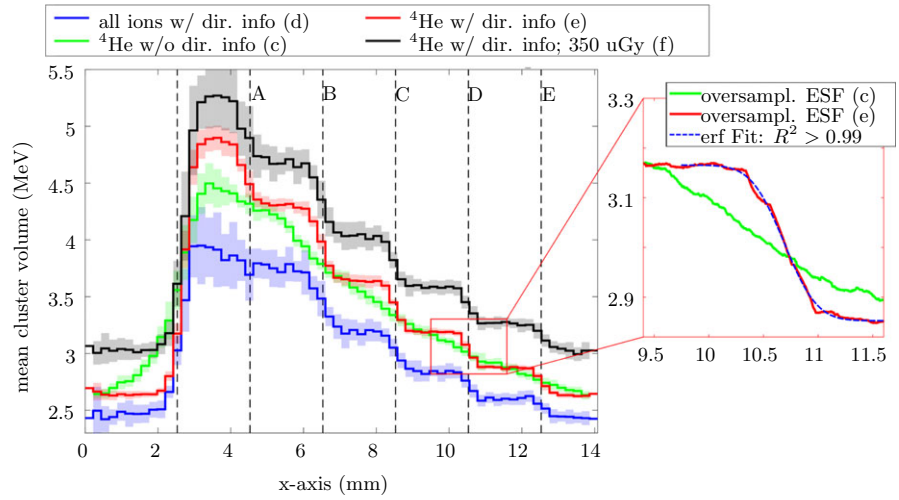

FIG. 7. Averaged line-profiles along the *x*-axis of the images in Figs. 6(c)–6(f). The averaging along the *y*-axis was performed over pixel row 10–29 of Fig. 6. The shaded areas of the three curves indicate the standard deviation of the average values. The black, dashed vertical lines (A, B, C, D, E) indicate the positions of the step edges, having a distance of 2 mm to each other. For visibility, the black curve was shifted by 0.4 MeV in the vertical direction. The magnification shows two examples of oversampled ESFs for the images (c) and (e), whereas the latter was fitted by an error function to determine the spatial resolution. [Color figure can be viewed at wileyonlinelibrary.com]

TABLE I. The CNR and the spatial resolution determined experimentally at the step transitions in the images (c)–(f) of Fig. 7. Spatial resolution is only shown for the final image (f), since the evaluation of image (e), obtained with a higher dose, yields similar results. * and ** indicate that the CNR and the spatial resolution could not be evaluated, respectively (see text for details).

	Step transition				
CNR	A	B	C	D	E
^{4}He w/ dir. info; 350 μGy (f)	1.7(1)	3.7(2)	3.6(1)	3.7(1)	2.7(1)
^{4}He w/ dir. info; 2200 μGy (e)	4.2(1)	7.7(4)	6.8(10)	7.5(10)	6.1(4)
all ions w/ dir. info; 2200 μGy (d)	0.4(0)	3.1(1)	2.6(1)	2.5(2)	1.8(1)
^{4}He w/o dir. info; 2200 μGy (c)	*	*	*	*	*
$MTF_{10\%}$(lp mm^{-1})	A	B	C	D	E
^{4}He w/ dir. info; 350 μGy (f)	1.23(18)	1.15(4)	1.24(8)	1.39(4)	1.30(6)
^{4}He w/o dir. info; 2200 μGy (c)	**	**	**	**	**

identification of single ions. The measurements were performed with silicon pixel detectors. To our knowledge, it is one of the first helium-beam radiographs in general and the first helium-beam radiograph that has been performed with thin silicon pixel detectors in particular. Prior experimental works related to helium-beam radiography comprise an early work based on a passive radiation detection with films[57] or a work about heavy ion CT performed with a detection system integrating the measured signal over the course of the irradiation,[18] so that no information about single ion tracks was measured. The present work showed the experimental feasibility of helium-beam radiography with the introduced detection system, being an active method with the capability of single ion detection.

Nuclear fragmentations of the primary helium ions, mainly taking place within the object being imaged, lead to the production of secondary hydrogen ions, also reaching the detection system. In the measurements, the secondary hydrogen ions accounted for 14% of all tracks measured by all three detection layers. They would have "diluted" the image due to their lower stopping power in comparison to helium ions and were therefore identified and rejected. The differentiation between helium ions and hydrogen ions, suggested in this work, is based on the large difference in their cluster volume, that is, energy deposition, and in their cluster size. A limitation of this method might occur for objects with a large WET modulation, where the energy deposition of a hydrogen ion could be equal or even bigger than the energy deposition of a helium ion (passing through a large and small WET, respectively). However, a comparison of the corresponding Bragg curves for helium ions and protons shows that a WET difference of approximately 100 mm would be necessary to obtain the same energy deposition for the two different ion types (see, for example, Burigo et al.[38]). For deuterium and tritium ions, the WET difference would have to be even larger, since their range is two and three times larger than the one of protons, respectively. Such a large WET difference is unlikely to be present in small regions of, for example, 200 mm^2. Hence, the differentiation based on energy deposition is expected to work for small images or even for larger images if the differentiation is locally performed in several small regions of the image. Since the identification of helium and hydrogen ions is performed in a single detection layer with a WET below 1 mm, it might be easily integrated into other detection systems for iRad or iCT.

The tracking and backprojection of the single helium ions was shown to distinctly improve the spatial resolution. It can be seen by the fact that the 2 mm wide steps could be clearly resolved for the images with tracking, while they could not be separately perceived in the images without tracking. The

tracking of the ions is of importance, as the MCS of the helium ions — although less pronounced than for protons — plays a not negligible role for helium-beam radiography.[18,30] This is in contrast to carbon ion imaging, where many detection systems were developed without tracking capabilities based on the assumption that the image blurring due MCS of carbon ions is sufficiently small.[19,20,58]

The presented detection system that allows helium ion tracking behind the object leads to good spatial resolutions ($MTF_{10\%} > 1.15$ lp mm^{-1}) in the case, where the feature of interest is located at the rear of the object. In cases, where the feature of interest is located in front or in the middle of the phantom, the spatial resolution is stronger affected by MCS than in the aforementioned case. In the course of an eventual clinical translation of the reported helium-beam radiography, an additional measurement of the position and direction of the helium ions in front of the object could be implemented as already pointed out in several works about proton tomography.[22,27,32] The trajectory information of the particle could then be used in *most likely path* (MLP) algorithms for the optimization of the spatial resolution.[23–26]

The helium-beam radiograph at a clinical dose level showed high CNR values (> 3.5) for relative thickness differences of 1.2% in a WET range of the phantom of approximately 6 mm × $WEPL_{PMMA} \approx 7$mm. The upper limit of this range is given by the WET, at which the emerging ions are close to the end of their range in the last thin detection layer. Due to the associated steep decrease in the fluence, the CNR is significantly decreased. The lower limit of this WET range is caused by the decreasing gradient of the Bragg curve at the position of detector 1 for decreasing WET. The decrease in the gradient leads to a smaller contrast and thus to a smaller CNR, as shown in Table I by the CNR on the right (step transition E). To address that, the residual energy/range could be measured as an additional parameter, as described, for example, in Bashkirov et al. and Amaldi et al.[29,33]. Also conceivable is the measurement of the energy deposition in several Timepix detector layers behind the object, possibly interleaved with some build-up material. Here, the tracking system consisting of two detector layers without build-up material could be placed upstream of the interleaved energy detectors, so that the MCS in the build-up material does not affect the track information.

For a possible clinical application of the presented methodology, the field of view has to be increased. Different vendors already offer Timepix detectors with a sensitive area up to 140 mm × 140 mm. However, issues to be addressed for large-area, multilayered Timepix or Timepix3 detection systems are a low material budget between the sensitive layers and an efficient cooling system.

A further issue to be addressed is the currently too long dead time of approximately 82 ms per 1 ms acquisition time. This dead time is not problematic with respect to the delivered dose, since the ion beam at HIT can be synchronized with the detection system such that the irradiation is halted during dead times. However, the dead time limited the particle detection rate to approximately 800 Hz and led to a long acquisition time of 5.9 min (including detector dead times and accelerator spill pauses) for the radiograph in Fig. 6(f). The next generation of the Timepix chip — Timepix3 — provides a distinctly faster readout due to data-driven and sparse readout of the pixel matrix enabling much higher throughput of up to 80 Mhits/s.[59] This throughput is given for homogeneously distributed single-pixel clusters and would translate into a promising particle detection rate >1 MHz for measurements with 20-pixel clusters.

5. SUMMARY AND CONCLUSION

This paper reports on a feasibility study of helium-beam radiography with the introduced detection system consisting of three thin pixelated silicon detectors with parallel alignment. A methodology of helium-beam radiography, which is based on energy deposition measurements of single ions in thin layers, together with tracking and identification of the ions leaving the imaged object, was described. The steep gradient in energy deposition proximal to the Bragg peak was exploited in order to optimize the thickness resolution of the radiographic images.

A key prerequisite for the image formation was the development of a data-processing procedure. It excluded detector artifacts and signals that were degraded due to incomplete electronic readout.

The noise of the image was shown to be reduced by identifying and excluding secondary hydrogen ions, which accounted for 14% of all tracks measured by the three detection layers. The improvement of the CNR by at least a factor of 2.5 experimentally demonstrated that the identification of secondary ions plays an important role for helium-beam radiography. Additionally, the spatial resolution of the image was improved by considering the directional information of the helium ions leaving the phantom. A minimal spatial resolution of $MTF_{10\%} = 1.15$ lp mm^{-1} for the presented experimental set-up and an image reconstruction in a certain plane of interest was demonstrated.

A WET resolution sufficient to resolve relative thickness differences of 1.2% (with a CNR between 1.7 and 3.7) at a maximal overall PMMA thickness of 170 mm was achieved at a dose level of diagnostic x-ray images with an average dose of 350 mGy.

ACKNOWLEDGMENTS

The authors thank the HIT facility for the beam time and especially Dr. Stephan Brons for the great help with the beam-time preparation. We also thank the accelerator team at HIT for their readiness to finetune the beam for our needs. Furthermore, we thank Dr. Jan Jakubek, Daniel Turecek, Dr. Pavel Soukup and the whole team of Advacam s.r.o. for the support concerning the Timepix and FitPIX devices, and Gernot Echner and the workshop at DKFZ for the construction of the detector support and the phantom. TG was funded by the German Science Foundation (DFG). MM was funded by the

German Cancer Aid (Deutsche Krebshilfe). This work was supported by the DFG (KFO 214, under the project number MA 4437/3-1).

CONFLICTS OF INTEREST

The authors have no relevant conflicts of interest to disclose.

*Present address: Physikalisch-Technische Bundesanstalt (PTB), Bundesallee 100 38116, Braunschweig, Germany.
[a)]Author to whom correspondence should be addressed. Electronic mail: t.gehrke@dkfz.de

REFERENCES

1. Schardt D, Elsässer T, Schulz-Ertner D. Heavy-ion tumor therapy: physical and radiobiological benefits. *Rev Mod Phys*. 2010;82:383–425.
2. Schulz-Ertner D, Tsujii H. Particle radiation therapy using proton and heavier ion beams. *J Clin Oncol*. 2007;25:953–964.
3. Yang M, Zhu XR, Park PC, et al. Comprehensive analysis of proton range uncertainties related to patient stopping-power-ratio estimation using the stoichiometric calibration. *Phys Med Biol*. 2012;57:4095–4115.
4. Paganetti H. Range uncertainties in proton therapy and the role of Monte Carlo simulations. *Phys Med Biol*. 2012;57:R99–117.
5. Cormack AM. Representation of a function by its line integrals, with some radiological applications. *J Appl Phys*. 1963;34:2722–2727.
6. Schulte R, Bashkirov V, Li T, et al. Conceptual design of a proton computed tomography system for applications in proton radiation therapy. *IEEE Trans Nucl Sci*. 2004;51:866–872.
7. Poludniowski G, Allinson NM, Evans PM. Proton radiography and tomography with application to proton therapy. *Br J Radiol*. 2015;88:20150134. PMID: 26043157.
8. Mumot M, Algranati C, Hartmann M, Schippers JM, Hug E, Lomax AJ. Proton range verification using a range probe: definition of concept and initial analysis. *Phys Med Biol*. 2010;55:4771.
9. Schneider U, Besserer J, Pemler P, et al. First proton radiography of an animal patient. *Med Phys*. 2004;31:1046–1051.
10. Crowe KM, Budinger TF, Cahoon JL, Elischer VP, Huesman RH, Kanstein LL. Axial Scanning with 900 MeV Alpha Particles. *IEEE Trans Nucl Sci*. 1975;22:1752–1754.
11. Benton EV, Henke RP, Tobias CA. Heavy-particle radiography. *Science*. 1973;182:474–476.
12. Schneider U, Pemler P, Besserer J, Pedroni E, Lomax A, Kaser-Hotz B. Patient specific optimization of the relation between CT-Hounsfield units and proton stopping power with proton radiography. *Med Phys*. 2005;32:195–199.
13. Doolan PJ, Testa M, Sharp G, Bentefour EH, Royle G, Lu H-M. Patient-specific stopping power calibration for proton therapy planning based on single-detector proton radiography. *Phys Med Biol*. 2015;60:1901.
14. Testa M, Verburg JM, Rose M, et al. Proton radiography and proton computed tomography based on time-resolved dose measurements. *Phys Med Biol*. 2013;58:8215.
15. Doolan PJ, Royle G, Gibson A, Lu H-M, Prieels D, Bentefour EH. Dose ratio proton radiography using the proximal side of the Bragg peak. *Med Phys*. 2015;42:1871–1883.
16. Rinaldi I, Brons S, Gordon J, et al. Experimental characterization of a prototype detector system for carbon ion radiography and tomography. *Phys Med Biol*. 2013;58:413.
17. Zygmanski P, Gall KP, Rabin MSZ, Rosenthal SJ. The measurement of proton stopping power using proton-cone-beam computed tomography. *Phys Med Biol*. 2000;45:511.
18. Muraishi H, Nishimura K, Abe S, et al. Evaluation of spatial resolution for heavy ion CT system based on the measurement of residual range distribution with HIMAC. *IEEE Trans Nucl Sci*. 2009;56:2714–2721.
19. Telsemeyer J, Jäkel O, Martišková M. Quantitative carbon ion beam radiography and tomography with a flat-panel detector. *Phys Med Biol*. 2012;57:7957.
20. Meyer S, Gianoli C, Magallanes L, et al. Comparative Monte Carlo study on the performance of integration- and list-mode detector configurations for carbon ion computed tomography. *Phys Med Biol*. 2017;62:1096.
21. Schneider U, Pedroni E. Proton radiography as a tool for quality control in proton therapy. *Med Phys*. 1995;22:353–363.
22. Johnson RP, Bashkirov V, DeWitt L, et al. A fast experimental scanner for proton CT: technical performance and first experience with phantom scans. *IEEE Trans Nucl Sci*. 2016;63:52–60.
23. Williams DC. The most likely path of an energetic charged particle through a uniform medium. *Phys Med Biol*. 2004;49:2899.
24. Schulte RW, Penfold SN, Tafas JT, Schubert KE. A maximum likelihood proton path formalism for application in proton computed tomography. *Med Phys*. 2008;35:4849–4856.
25. Schneider U, Pedroni E, Hartmann M, Besserer J, Lomax T. Spatial resolution of proton tomography: methods, initial phase space and object thickness. *Zeitschrift für Medizinische Physik*. 2012;22:100–108.
26. Fekete CAC, Doolan P, Dias MF, Beaulieu L, Seco J. Developing a phenomenological model of the proton trajectory within a heterogeneous medium required for proton imaging. *Phys Med Biol*. 2015;60:5071.
27. Sipala V, Bruzzi M, Bucciolini M, et al. A proton computed tomography system for medical applications. *J Instrum*. 2013;8:C02021.
28. Amaldi U, Bianchi A, Chang Y-H, et al. Construction, test and operation of a proton range radiography system. *Nucl Instrum Methods Phys Res A*. 2011;629:337–344.
29. Poludniowski G, Allinson NM, Anaxagoras T, et al. Proton-counting radiography for proton therapy: a proof of principle using CMOS APS technology. *Phys Med Biol*. 2014;59:2569.
30. Collins-Fekete C-A, Volz L, Portillo SKN, Beaulieu L, Seco J. A theoretical framework to predict the most likely ion path in particle imaging. *Phys Med Biol*. 2017;62:1777.
31. Plautz TE, Bashkirov V, Giacometti V, et al. An evaluation of spatial resolution of a prototype proton CT scanner. *Med Phys*. 2016;43:6291–6300.
32. Bashkirov VA, Schulte RW, Hurley RF, et al. Novel scintillation detector design and performance for proton radiography and computed tomography. *Med Phys*. 2016;43:664–674.
33. Highland VL. Some practical remarks on multiple scattering. *Nucl Instrum Methods*. 1975;129:497–499.
34. Lynch GR, Dahl OI. Approximations to multiple Coulomb scattering. *Nucl Instrum Methods Phys Res B*. 1991;58:6–10.
35. Seltzer SM, Berger MJ. Energy loss straggling of protons and mesons: tabulation of the vavilov distribution. In: National Research Council (US), ed. *Studies in Penetration of Charged Particles in Matter*. Washington, DC: National Academies; 1964:187.
36. Patrignani C, Group particle data. *Rev Part Phys Chin Phys C*. 2016;40:100001.
37. Bethe H, Heitler W. On the stopping of fast particles and on the creation of positive electrons. *Proc R Soc Lond A: Math Phys Eng Sci*. 1934;146:83–112.
38. Burigo L, Pshenichnov I, Mishustin I, Bleicher M. Microdosimetry spectra and RBE of 1H, 4He, 7Li and 12C nuclei in water studied with Geant4. *Nucl Instrum Methods Phys Res B*. 2014;320:89–99.
39. Combs SE, Ellerbrock M, Haberer T, et al. Heidelberg ion therapy center (HIT): initial clinical experience in the first 80 patients. *Acta oncol*. 2010;49:1132–1140.
40. Jermann M. *Particle therapy patient statistics (per end of 2015)*. http://www.ptcog.ch/index.php/patient-statistics. Accessed November 30, 2017.
41. Weber U, Kraft G. Design and construction of a ripple filter for a smoothed depth dose distribution in conformal particle therapy. *Phys Med Biol*. 1999;44:2765.
42. Llopart X, Ballabriga R, Campbell M, Tlustos L, Wong W. Timepix, a 65k programmable pixel readout chip for arrival time, energy and/or photon counting measurements. *Nucl Instrum Methods Phys Res A*. 2007;581:485–494.
43. Gehrke T, Burigo L, Arico G, et al. Energy deposition measurements of single 1 H, 4 He and 12 C ions of therapeutic energies in a silicon pixel detector. *J Instrum*. 2017;12:P04025.

44. Kraus V, Holik M, Jakubek J, Kroupa M, Soukup P, Vykydal Z. FITPix—fast interface for Timepix pixel detectors. *J Instrum*. 2011;6:C01079.
45. Soukup P, Jakubek J, Vykydal Z. 3D sensitive voxel detector of ionizing radiation based on Timepix device. *J Instrum*. 2011;6:C01060.
46. Turecek D, Holy T, Jakubek J, Pospisil S, Vykydal Z. Pixelman: a multi-platform data acquisition and processing software package for Medipix2, Timepix and Medipix3 detectors. *J Instrum*. 2011;6:C01046.
47. Jakubek J. Precise energy calibration of pixel detector working in time-over-threshold mode. *Nucl Instrum Methods Phys Res A*. 2011;633(Suppl 1):S262S266.
48. Jakubek J. *Detector response to highly energetic particles–charge collection model*. In 3rd Annual ARDENT Workshop; 2014.
49. Hartmann B, Soukup P, Granja C, et al. Distortion of the per-pixel signal in the Timepix detector observed in high energy carbon ion beams. *J Instrum*. 2014;9:P09006.
50. Fujita H, Tsai DY, Itoh T, et al. A simple method for determining the modulation transfer function in digital radiography. *IEEE Trans Med Imaging*. 1992;11:34–39.
51. Bushberg JT, Seibert JA, Leidholdt EM, Boone JM. *The Essential Physics of Medical Imaging*. Philadelphia, PA: Wolters Kluwer Health; 2011.
52. Ferrari A, Sala Paola R, Fassò A, Ranft J. *FLUKA: A multi-particle transport code*. Geneva: CERN 2005-10, INFN/TC_05/11, SLAC-R-773 2005.
53. Böhlen TT, Cerutti F, Chin MPW, et al. The FLUKA Code: developments and challenges for high energy and medical applications. *Nucl Data Sheets*. 2014;120:211–214.
54. Schegerer AA. *Bekanntmachung der aktualisierten diagnostischen Referenzwerte für diagnostische und interventionelle Röntgenanwendungen*. Bundesamt für Strahlenschutz, 2016. http://www.bfs.de/EN/topics/ion/medicine/diagnostics/reference-values/reference-values_node.html. Accessed November 30, 2017.
55. Benmakhlouf H, Fransson A, Andreo P. Influence of phantom thickness and material on the backscatter factors for diagnostic x-ray beam dosimetry. *Phys Med Biol*. 2013;58:247.
56. Hubbell JH, Seltzer SM. *Tables of x-ray mass attenuation coefficients and mass energy-absorption coefficients (version 1.4)*. National Institute of Standards and Technology, Gaithersburg, MD, 2004. http://physics.nist.gov/xaamdi. Accessed March 10, 2017.
57. Budinger TF, Crowe K, Kanstein LL. *Preliminary experiments with helium ion radiography at the 184-inch cyclotron*. tech. rep. Lawrence Berkeley Laboratory, University of California, Berkeley, USA 1974.
58. Rinaldi I, Brons S, Jäkel O, Voss B, Parodi K. Experimental investigations on carbon ion scanning radiography using a range telescope. *Phys Med Biol*. 2014;59:3041.
59. Poikela T, Plosila J, Westerlund T, et al. Timepix3: a 65K channel hybrid pixel readout chip with simultaneous ToA/ToT and sparse readout. *J Instrum*. 2014;9:C05013.